3D arrays of 1D MnO_2 nanocrystals for all solid state asymmetric supercapacitors

Deepak P. Dubal[a,b]*, *Rudolf Holze*[b], *Pedro Gomez-Romero*[a,c]**

[a]Catalan Institute of Nanoscience and Nanotechnology, CIN2, ICN2 (CSIC-ICN), Campus UAB, E-08193 Bellaterra, Barcelona, Spain

[b]Technische Universität Chemnitz, Institut für Chemie, AG Elektrochemie, D-09107 Chemnitz, Germany

[c]Consejo Superior de Investigaciones Científicas (CSIC), Spain

CORRESPONDING AUTHOR FOOTNOTE

Dr. Deepak Dubal, and Prof. Pedro Gomez-Romero

Tel.: +349373609/+345929950 Fax: +345929951

E-mail: dubaldeepak2@gmail.com (D. Dubal),

pedro.gomez@cin2.es (P. Gomez-Romero)

Abstract

We report the synthesis of 3D hierarchical structures based on 1D MnO_2 nano-building blocks (nanorods, nanowires and nanoneedles) via a facile and scalable co-precipitation method and their use as electrodes for the assembly of all-solid-state supercapacitors. Symmetric supercapacitors were assembled and tested. But also asymmetric devices were assembled by using those nanostructured MnO_2 materials as the positive electrode and reduced graphene oxide (rGO) as the negative electrode with polymeric gel electrolyte. These asymmetric cells successfully extend the working voltage windows beyond 1.4 V and in our case allowed for a maximum voltage of 1.8 V. An asymmetric device based on hierarchical nanoneedle-like MnO_2 and rGO achieved a maximum specific capacitance of 99 F/g at scan rate of 10 mV/s with a stable operational voltage of 1.8 V. This high value allowed for a large specific energy of 24.12 Wh/kg.

1. Introduction

The spectacular evolution from portable to wearable electronics, the consolidation of e-paper and other flexible devices, entails power sources with greater flexibility on top of high-performance low cost and long cycle life [1]. In this field, flexible all solid state supercapacitors (ASSSs) (SSSCs) (ASSSCs) are the rising stars among these emerging energy storage technologies due to their excellent flexibility and high safety [2]. These all solid state supercapacitors (ASSSs) are compact, sustainable, mobile and robust over long periods of time. Electrode materials can be of two types depending on their charge-storing mechanisms, namely, electric double-layer capacitors (EDLCs) (mostly carbon materials) and pseudocapacitors (PCs) (either transition metal oxides or conducting polymers), whereas solid gel electrolytes are commonly used in ASSSs [3]. The use of solid electrolytes in supercapacitors have several advantages over liquid ones that include ease of handling without spilling of hazardous liquids, thus making them environmentally safe, but also low internal corrosion, simple principle and mode of construction, flexibility in packaging etc. [4] On the other hand, the design of ASSSs with high capacitance, high energy-density and good cycling performance is still a challenge due to relatively low capacitance of EDLCs and low conductivity of pseudo-capacitive materials.

The use of nanoscaled particles significantly enhances the performance of supercapacitive materials by improving structural interfaces, leading to enhanced charge transfer, and shortening drastically the ion/electron diffusion pathways by decreasing the grain size of the bulk material [5]. Among nanoscaled materials for supercapacitors MnO_2 is one of the most versatile due to the wide diversity of crystal structures, morphologies, porosity and textures available for this inexpensive and environmentally friendly material. These structural parameters play a crucial role in determining and optimizing the electrochemical properties of MnO_2 as

electrode material [6]. Extensive efforts have been dedicated to obtain different morphologies of MnO_2 including nanorods by hydrothermal or room temperature co-precipitation method, nanowires by hydrothermal, nanoflowers by hydrothermal, spherical urchins by hydrothermal etc. in order to improve its capacitance and power performance in supercapacitors [7]. However, some severe drawbacks still burden MnO_2 electrodes, including problems of aggregation, large interfacial resistance between adjacent particles, resulting in great supercapacitive losses and poor calendar life. To address these issues, an interesting and explored avenue is to efficiently construct one, two and three-dimensional (3D) interconnected hierarchical porous frameworks which could simultaneously provide a continuous electron transport path, a large electrode-electrolyte interface and efficient penetration and diffusion of the electrolyte [8]. Furthermore, these sophisticated MnO_2 electrode structures should not be the result of sophisticated synthetic methods if widespread industrial applications are sought. On the contrary, for mass production, facile, scalable and low-cost synthetic procedures should be developed.

The work reported here reports the facile synthesis of different nanostructures of MnO_2 and their use to assemble high-performance all-solid-state supercapacitors (ASSSs). There are three steps involved in this investigation, 1) synthesis of different nanostructures by co-precipitation method at 353 K, 2) fabrication of flexible electrodes by applying MnO_2 paste on flexible stainless steel substrates, 3) assembly of all solid state symmetric and asymmetric supercapacitors using PVA-H_3PO_4 gel electrolyte. The results evidenced the dependence of MnO_2 nanostructures on the supercapacitive performance of the device. As it will be shown, the asymmetric configuration significantly extends the maximum working voltage of the device up to 1.8 V providing high energy density.

2. Experimental details

2.1 Synthesis of MnO_2 nanostructures

Three different nanostructures of MnO_2 such as nanorods (Nr), nanowires (Nw) and nanoneedles (Nn) have been successfully synthesized by simple co-precipitation method. Briefly, 0.1 M $MnSO_4$ and 0. 1 M $(NH_4)_2S_2O_8$ were used as source of manganese and oxidizing agent, respectively. The nanostructures of MnO_2 were tuned by using 0.05 M $(NH_4)_2SO_4$ and 0.05 M NH_4F as templates. As a reference, MnO_2 without any template was also prepared. All these precursors were maintained at 353 K for 1 h. The products were filtered off, successively washed with water and ethanol and finally dried in an oven at 373 K overnight. Thus three different products were collected one prepared without and the other two with templates.

2.2 Synthesis of reduced graphene oxide (rGO)

2.5 g of graphite powder, 1.25 g of $NaNO_3$ and 60 mL of H_2SO_4 were mixed together with stirring for 30 min and cooled in an ice bath. 7.5 g of potassium permanganate was added slowly to this solution with continuous stirring overnight. Subsequently this solution was diluted with 100 mL of distilled water at high speed stirring. The temperature rapidly increased to 98 °C and was maintained there for 5 h. Then, 25 mL of 30 % H_2O_2 were added to this solution. The final product was washed several times with distilled water and HCl (97 %) and then re-suspended in distilled water. The aqueous graphite oxide solution was sonicated vigorously for 2 h to exfoliate the stacked graphite oxide sheets into monolayer or multi-layered graphene oxide sheets. The concentration of prepared graphene oxide solution is about 2 mg/ml. The rGO were synthesized by hydrothermal method. Thus, 50 ml of the above graphene oxide solution was sealed into a Teflon-lined stainless steel autoclave and heated at 180 °C for 5 h. This treatment converts graphene oxide into reduced graphene oxide (rGO).

2.2 Materials and electrochemical characterizations

X-ray diffraction (XRD) of solid samples was carried out using a Bruker AXS D8 Advance diffractometer with copper radiation (K_α of λ=1.54 Å). The microstructures of the MnO_2 nanostructures were investigated by scanning electron microscope (SEM, Nova NanoSEM 200). To obtain a typical slurry 85% of active material (MnO_2) was mixed with 10 % PVDF as binder and 5 % acetylene black. A fine mixture of active material, PVDF and acetylene black with NMP (solvent) was prepared. Finally the paste was applied on flexible stainless steel foil which was further used as supercapacitive electrodes. Electrochemical properties were investigated by assembling three-electrode cells comprising a working electrode (MnO_2 or rGO), counter electrode (platinum wire) and reference electrode (saturated calomel electrode (SCE)) in 1 M Na_2SO_4 electrolyte. An asymmetric supercapacitor cell was fabricated with MnO_2 as the positive electrode (cathode) and rGO coated on stainless steel foil as the negative electrode (anode) with H_3PO_4-PVA gel electrolyte. All electrochemical characteristics were evaluated by cyclic voltammetry (CV) and galvanostatic charge/discharge (CD) measurements on IviumStat and Atlas-0961 multichannel battery interface.

3. Results and discussion

It has been well documented that the nanostructures of electrode materials can influence the electrochemical performance of a device. Fig. 1 shows SEM images of the three MnO_2 products successfully synthesized, namely, nanorods (Mn-Nr), nanowires (Mn-Nw) and nanoneedles (Mn-Nn) at two different magnifications. MnO_2 prepared without any template forms microspherical aggregates of randomly oriented nanorods (see Fig. 1 (a, b)). Due to the one-dimensional growth tendency of α-MnO_2 crystals, epitaxial growth of nanorods from the

initial colloidal microsphere occurred, which resulted in the formation of spherical aggregation of nanorods. The nanorods located on the outside would act as nucleation centers for further crystallization. On the other hand, the use of $(NH_4)_2SO_4$ template, results in the formation of nanowires as seen from Fig. 1 (c, d). These nanowires are entangled with each other to form a porous network. Slim and long nanowires with an aspect ratio much larger than the nanorods described previously, serve both as the backbone and electron ‘‘superhighway’’ for charge storage and delivery while allowing for a large electrode/electrolyte contact interface. Finally, it is very interesting to note that the use of NH_4F during the deposition of MnO_2 leads to 3D urchin-like structures composed of large amounts of radially grown nanoneedles (Fig. 1 (e, f)). These nanoneedles are intercrossed and interconnected with one another, forming an intricate transportation network. NH_4F plays an essential role in the formation of this sort of morphology. When there is no assistance from templates such as $(NH_4)_2SO_4$ and NH_4F, only aggregated microspheres of nanorods was observed which suggests that these templates act as structure directing agents. Briefly, the partial hydrolysis of $(NH_4)_2SO_4$ and NH_4F produces ammonia which forms coordination complexes with Mn^{2+} and reduces the rate of crystal growth. As the reaction temperature increases, hydrolysis of more $(NH_4)_2SO_4$ and NH_4F molecules takes place. This increases the concentration of OH^- in the solution which directs the formation of thin nanowires and nanoneedles [9]. From a thermodynamic point of view, the surface energy of an individual nanowire or nanoneedle is relatively high and therefore they tend to aggregate perpendicularly to the surface planes in order to decrease the surface energy [10]. Therefore, as the reaction proceeds, the thin nanowires or nanoneedles would self-aggregate to form clustered MnO_2 nanostructures for minimizing the overall surface energy. In the case of NH_4F, the presence of F^- can stimulate the production of more active sites for nucleation and hence a high-

yield formation of nanoneedles takes place. Fig. 2 (a-c) shows TEM images of the different nanostructures of MnO_2 just described, further confirming the formation of nanorods, nanowires and spherical urchin-like MnO_2. Moreover, selected area electron diffraction pattern (SAED) along with HRTEM image of the edge of a nanoneedle is shown in Fig. 2 (d). The corresponding SAED pattern shows diffuse rings, indicating the polycrystalline nature of nanoneedles. The interplanar spacing was measured to be approximately 0.65 nm, which is in good agreement with the (110) crystalline plane of α-MnO_2 (inset of Fig. 2 (d)).

Despite its deceivingly simple formula, MnO_2 presents a rich variety of crystal structures all of them coming from one basic structural unit, MnO_6 octahedra. In the world of MnO_2, this little tiny MnO_6 octahedron enables the buildup of a colorful and diverse collection in which each phase is just the result of a given topological combination of MnO_6 octahedra. Fig. 3 shows the XRD patterns of the three different nanostructures of MnO_2 prepared (Mn-Nr, Mn-Nw and Mn-Nn). All the peaks recorded in these XRD patterns correspond to the α-MnO_2 crystal structure according to JCPDS no. 44-0141. This α-MnO_2 consists of interlinked double chains of octahedral MnO_6 and an interstitial space comprised of one-dimensional channels that extend in a direction parallel to the 'c' axis of a tetragonal unit cell. The electrochemical performance of MnO2 oxides is strongly dependent on their crystallographic form [11]. Previous results suggest that, α-MnO_2 provides the best suited crystallographic form for energy storage due to the large tunnel size which favors the storage of ions as compared to small tunnel of β-MnO_2 [12]. To investigate the nature of the MnO_2, we conducted FT-IR analysis (supporting information S1). The peaks at 767, 620 and 529 cm^{-1} are deemed as the main characteristic absorption bands of MnO_2, which corresponds to the Mn-O stretching modes of the octahedral sites.

To further investigate the surface property of all three nanostructures of MnO_2, we measured the Brunnauer-Emmett-Teller (BET) and nitrogen adsorption-desorption, as shown in Fig. 4 (a). All three nanostructures show typical type IV isotherm with hysteresis loops in a relative pressure (P/P_0) range of 0.4-1.0, implying the formation of mesopores structures. The average pore diameters of nanorods, nanowires and urchin-like structures of MnO_2 samples are found to be in the mesopore region as seen from Fig. 4 (b). The intensities of the pore size distribution in Mn-Nn sample are slightly higher than that of Mn-Nr and Mn-Nw samples suggesting higher pore volume of Mn-Nn sample. The meso-porosity of MnO_2 samples is an amalgamation of internal space of the agglomerated nanostructures, surface porosity and the porosity due to internal space of the nanostructures. The BET surface area Mn-Nr, Mn-Nw and Mn-Nn samples are 49, 58 and 67 m^2/g, respectively. Thus the nano-needle MnO_2 possess highest surface area as compared to other two nanostrcutures. Such 3D hierarchical nanostructure with high surface area and meso-porous structure is advantageous for energy storage applications since large pore channels permit rapid electrolyte transport, while the small pores provide more active sites for chemical reactions.

In order to further explore the importance of nanostructures, the electrochemical and supercapacitive properties of three MnO_2 products were investigated by assembling three electrode cells. Fig. 5 (a-c) shows the CV curves of Mn-Nr, Mn-Nw and Mn-Nn electrodes at different scanning rates, respectively. It can be clearly observed that the CV curves of all the three MnO_2 samples show similar rectangular shapes (capacitive behavior) but with increased currents in the order of Mn-Nr < Mn-Nw < Mn-Nn, which might be related to the different nanostructures of the samples. The CV curves highlight a clear dependence of scan rate due to the continuous increase in area under the curves with scan rate. Moreover, the shapes of CV

curves maintain their rectangular shapes even under high scanning rates of 200 mV/s, indicating that the faradaic redox reactions are electrochemically reversible [13]. The specific capacitance of MnO_2 electrodes can be estimated by the following equation:

$$C = \frac{1}{\nu(V_c - V_a)m}\int_{V_a}^{V_c} I_m dV \qquad (1)$$

where C is the specific capacitance (F/g), ν is the potential scan rate (mV/s), V_c-V_a is the voltage window and I_m denotes the response current (A/g). At potential scan rates of 10 mV/s, the specific capacitances obtained for Mn-Nr, Mn-Nw and Mn-Nn electrodes are found to be 282 F/g (2.1 mg/cm^2), 322 F/g (2.2 mg/cm^2) and 368 F/g (2.1 mg/cm^2), respectively. The values reported are comparable or little higher than that reported for other nanostructures of MnO_2 by other different methods (supporting information S2). As it could be expected, the CV data shows that there is a gradual decrease in the specific capacitance values with increase in scan rate (supporting information S3).

Galvanostatic charge-discharge curves of Mn-Nr, Mn-Nw and Mn-Nn at different current densities are shown in Fig. 5 (d-f), respectively. It can be seen that all of the curves are not ideal straight lines, indicating the involvement of a faradaic reaction (pseudocapacitance). Moreover, there is an initial drop in voltage, which is caused by internal resistance of the material. As seen from the Fig. 5, almost the same loss in initial voltage is observed for Mn-Nr and Mn-Nw samples while that for Mn-Nn sample is much smaller. The values of specific capacitances for MnO_2 electrodes have been calculated from the voltage-time measurements (excluding internal resistance drop) at different applied current densities using the following equation:

$$C_s = \frac{I\Delta t}{m\Delta V} \qquad (2)$$

where I (A/g) is the discharge current density for the applied time duration Δt (s), ΔV (V) is the voltage window, and m is the weight of the MnO_2 active materials.

To further improve the supercapacitive performances of MnO_2 nanostructures, asymmetric supercapacitors with MnO_2 as positive and carbon material (reduced graphene oxide, rGO) as negative electrodes with PVA-H_3PO_4 gel electrolyte have been fabricated to achieve a higher cell voltage, thanks to the high hydrogen evolution over-potential of carbon materials (rGO) in aqueous media. In these asymmetric cells charges are stored non-faradaically in rGO electrodes, and through redox reactions in MnO_2 electrodes. For instance, reduced graphene oxide (rGO) has been prepared by modified Hummer's method, reported elsewhere [14]. Thin and curly nanosheets are successfully formed (for details see supporting information S4). The cyclic voltammetry (CV) curves of rGO electrode can be operated over a wide range of scan rates: from 5 up to 200 mV/s in three electrodes configuration showing ideal electrochemical double layer behavior. Thus, the results demonstrate that rGO electrode exhibit high EDLC performance and would be a promising energy storage electrode material. The specific capacitance of the rGO electrode was found to be 122 F/g (1.9 mg/cm^2) at the scan rate of 5 mV/s (supporting information S4). Note that in order to reach the highest cell voltage, the charges stored in both electrodes must be balanced by adjusting the mass loading of the electrodes. The positive to negative electrode mass ratio was calculated by the following equation to achieve a charge balance $q^+ = q^-$.

$$\frac{m_+}{m_-} = \frac{(C_- \times \Delta E_-)}{(C_+ \times \Delta E_+)} \qquad (3)$$

where q^+, q^-, m_+, m_-, C_+, C_-, E_+, and E_- are the charge, mass, specific capacitance and potential windows for the cathode (+) and anode (-). Thus, optimal mass ratios between the positive and

negative electrodes of Mn-Nr//rGO (2.81 mg/cm^2//1.88 mg/cm^2), Mn-Nw//rGO (2.92 mg/cm^2//1.98 mg/cm^2) and Mn-Nn//rGO (3.43 mg/cm^2//1.76 mg/cm^2) were used. It is interesting to note that for Mn-Nr//rGO, Mn-Nw//rGO and Mn-Nn//rGO devices, the allowed working voltage windows are 0-1.7 V, 0-1.4 and 0-1.8 V, respectively. Above these limits the shapes of the CV curves looks somewhat distorted which may be due to hydrogen and/or oxygen evolution (supporting information S5). Moreover, the shapes of CV curves demonstrate an ideal capacitive behavior with small but obvious redox peaks, even at wide voltage window. It was further found that the current and consequently the specific capacitance greatly increase as the operating voltage window is increased, which indicates the improvement in stored energy and delivered power. The enhancement of the cell voltage will be a critical factor to improve the energy density of the Mn-X//rGO (X = Nr or Nw or Nn) asymmetric devices. Fig. 6 (a-c) shows the CV curves of Mn-Nr//rGO, Mn-Nw//rGO and Mn-Nn//rGO asymmetric devices at various scan rates ranging from 10 mV/s to 500 mV/s, respectively. Obviously, all the CV curves behave similarly in shape and the current density increases with scan rates. Even at a scan rate as high as 500 mV/s, the CV curves still has obvious redox peaks in the charge and discharge processes, indicating the superior high rate capability of present supercapacitor cells for the fast charge and discharge. Particularly noteworthy is that the CV integrated area of the Mn-Nn//rGO asymmetric cell is apparently larger than that of the other Mn-Nr//rGO and Mn-Nw//rGO cells with highest voltage window (1.8 V), indicating that the Mn-Nn//rGO cell has a significantly larger specific capacitance. The maximum specific capacitance values for Mn-Nr//rGO, Mn-Nw//rGO and Mn-Nn//rGO asymmetric cells are found to be in the range of 69 F/g, 80 F/g and 99 F/g, respectively at the scan rate of 10 mV/s. Remarkably, up to 33 %, 39 % and 50 % of capacitance is retained

when the scan rate is increased 20 times from 10 to 200 mV/s, indicating the very good high-rate performance of these asymmetric devices.

Fig. 6 (d-f) shows the Charge-Discharge curves for the Mn-Nr//rGO, Mn-Nw//rGO and Mn-Nn//rGO asymmetric cells at different current densities. As illustrated in Fig. 6 (d-f), the shapes of the CD curves for the all three asymmetric cells at different current densities tend towards triangular-shaped curves with very small initial voltage drop and the discharge curves are nearly symmetric with the corresponding charge counterparts, suggesting a rapid I-V response and good electrochemical reversibility. Additionally, it is worth noting that the Mn-Nn//rGO asymmetric cell demonstrates longer discharging time than the Mn-Nr//rGO, Mn-Nw//rGO. This confirms that the Mn-Nn//rGO asymmetric cell exhibits higher specific capacitance values than that of the other two cells. Moreover, the specific capacitances of the cells decrease with increasing current density (see Fig. 7 (a)). The reduction of specific capacitance at high scan rate and large current density can be attributed to the low diffusion of the electrolyte ion. The ionic motion in the electrolyte during the high rate charge-discharge process is always limited by diffusion, because of the time constraint, and only the outer active surface is utilized for charge storage, so there is an obvious reduction in the electrochemical utilization of the electroactive materials at high scan rates and large current densities [15].

Power density and energy density are the two significant parameters to characterize the performance of the supercapacitors. The CD curves are further utilized to evaluate the specific power and specific energy of Mn-Nr//rGO, Mn-Nw//rGO and Mn-Nn//rGO asymmetric cells. Fig. 7 (b) shows the Ragone plots of the present asymmetric device based on CD tests. It is worth noting that the maximum values of specific energy for Mn-Nr//rGO, Mn-Nw//rGO and Mn-Nn//rGO asymmetric cells are 14.31, 19.97 and 24.12 Wh/kg whereas the maximum specific

powers are 5.1, 6.2 and 7.8 kW/kg, respectively. Significantly, the specific energy obtained is higher than that of symmetrical supercapacitors such as CNTs//CNTs supercapacitors (<10 Wh/kg) [16], graphene/MnO_2//graphene/MnO_2 supercapacitors (8.1 Wh/kg) [17], AC//AC supercapacitors (<10 Wh/kg) [18], rGO//rGO supercapacitors (<4 Wh/kg) [19], and 3D graphene/MnO_2//3D graphene/MnO_2 (6.8 Wh/kg) [20]. Furthermore, we also compare the specific energy and power density of the all-solid-state devices. The maximum energy density of Mn-Nn//rGO (24.12 Wh/kg) at a current density of 2 A/g is larger than that previously reported for other manganese-oxides-based asymmetric supercapacitors in aqueous electrolytes, including activated carbon//mesoporous MnO_2 (10.4 Wh/kg at 0.3 A/g) [21], activated carbon//$NaMnO_2$ (19.5 Wh/kg at 0.04 A/g) [22], activated carbon//MnO_2 (17.3 Wh/kg at 0.55 A/g) [23], CNT//graphene-MnO_2 (12.5 Wh/kg at 0.45 A/g) [24], and graphene//graphene-MnO_2 (21.27 Wh/kg at 0.223 A/g) [25]. Moreover, in great contrast to supercapacitors packed with aqueous or organic electrolytes, the all-solid-state asymmetric supercapacitor of MnO_2//rGO using the polymer gel electrolytes exhibits excellent flexibility (see supporting information S6).

Cycling performance is the final key factor determining the viability of supercapacitors for many practical applications. In this study, a long-term cycle stability study of Mn-Nr//rGO, Mn-Nw//rGO and Mn-Nn//rGO asymmetric cells was carried out by repeating the CV tests at a scan rate of 100 mV/s for 5000 cycles (see supporting information S7). It can be clearly seen that the specific capacitance of asymmetric cells slightly decreases with cycles. The overall specific capacitance retention values for the Mn-Nr//rGO, Mn-Nw//rGO and Mn-Nn//rGO asymmetric cells were found to be 84%, 86% and 91 % after 5000 cycles, respectively (Fig. 8). The enhanced capacitive retention for Mn-Nn//rGO asymmetric cell is mainly attributed to their unique 3D nanoneedles-like structure which provides more active sites for efficient electrolyte

ion transport not only at the active materials surface but also throughout the bulk. These values are comparable to that of the porous NiO//carbon device (50% after 1000 cycles) [26], NiO//$Ru_{0.35}V_{0.65}O_2$ (83.5% after 1500 cycles) [27], $Ni(OH)_2$-MnO_2//rGO (76% after 3000 cycles) [28] and AC//$NiMoO_4.xH_2O$ (80.6% after 1000 cycles) [29].

Among the three different nanostructures of MnO_2 studied, the 3D urchin-like structure with sharp and slim nanoneedles exhibits excellent supercapacitive performance. These excellent performances are made possible by the unique design of hierarchical nanoneedles arrays which includes the following merits: 1) small diameters of the nanoneedles lead to a high surface area which surely contributes to the high capacitance, 2) well-defined and distinct structure of nanoneedles provides most of the surface easily accessible for electrolyte which will give high capacitance and enhanced electrochemical kinetics, 3) 1D nature of nanoneedles contributes to the cycling stability during the extended charge/discharge process, by facilitating the electron transfer and providing strong mechanical robustness. On the other hand, 1D nanorods and nanowires are self-aggregated to form clusters which significantly increase interfacial resistance between adjacent particles resulting in relative loss of supercapacitance.

Fig. 9 shows the schematic representation of asymmetric capacitor system according to the charge-potential profile. An asymmetric capacitor system is fabricated with a faradaic material (MnO_2) as positive and a non-faradic material (rGO) as negative electrode (see Fig. 9). Moreover, the voltage split depends on the capacitance of each electrode active material and can avoid the aqueous electrolyte decomposition at 1 V which occurs in the symmetric system. In an asymmetric system the potential remains constant (or slowly changing) for the faradaic electrode during charging due to redox reaction on the surface electrode. Therefore, it is essential to use a higher working potential combined with the non-faradic electrode at the initial stage of the

charging process resulting in an increase of the storable amount of energy compared to the symmetric system. Additionally, the surface redox reaction of the faradic electrode which shows slower kinetics than the electrostatic charge storage of the non-faradic electrode is still fast enough to operate as a counter electrode. Therefore, asymmetric capacitors can make full use of the different potential windows of the two electrodes to provide a maximum operating voltage in the cell system, thus resulting in a greatly enhanced specific capacitance and significantly improved energy density (Fig. 9).

4. Conclusions

Three different nanostructures of MnO_2 (nanorods, nanowires and nanoneedles) have been successfully synthesized by a scalable chemical co-precipitation method and have been used as electrode materials to set-up and test all-solid-state supercapacitors. First, all-solid-state asymmetric capacitors based on MnO_2//rGO were fabricated and tested. All the devices based on different nanostructures of MnO_2 show superb suspercapacitive performances. Asymmetric devices based on MnO_2//rGO are the most promising configuration, extending the working voltage windows beyond 1.4 V and achieving a maximum of 1.8 V. An asymmetric supercapacitor device based on hierarchical nanoneedle-like MnO_2 as the positive electrode and reduced graphene oxide (rGO) as the negative electrode can achieve a specific capacitance of 99 F/g at a scan rate of 10 mV/s with a stable operational voltage of 1.8 V and a maximum energy density of 24.12 Wh/kg. These results show that this type of asymmetric supercapacitor devices have a great potential for application as high energy density storage systems.

Acknowledgements

Authors appreciate the award to DPD of a Humboldt Fellowship of the Alexander von Humboldt Foundation (AvH), Germany and the award of a Marie-Curie Fellowship through Beatriu de Pinos Programme (BP-DGR-2013) for Catalan system of science and technology, Spain. ICN2 acknowledges support of the Spanish MINECO through the Severo Ochoa Centers of Excellence Program under Grant SEV-2013-0295.

References

[1] (a) D. P. Dubal, J. G. Kim, Y. Kim, R. Holze, C. D. Lokhande, W. B. Kim, *Energy Technol.*, **2014**, *2*, 325, (b) D. P. Dubal, O. Ayyad, V. Ruiz, P. Gomez-Romero, *Chem. Soc. Rev.* **2015**, DOI: 10.1039/c4cs00266k (c) H. Nishide, K. Oyaizu, *Science*, **2008**, *319*, 737, (d) L. Hu, Y. Cui, *Energy Environ. Sci.*, **2012**, *5*, 6423.

[2] (a) F. Meng, Y. Ding, *Adv. Mater.*, **2011**, *23*, 4098, (b) K. Wang, W. Zou, B. Quan, A. Yu, H. Wu, P. Jiang, Z. Wei, *Adv. Energy Mater.*, **2011**, *1*, 1068, (c) M. Kaempgen, C. K. Chan, J. Ma, Y. Cui, G. Gruner, *Nano Lett.*, **2009**, *9*, 1872.

[3] (a) D. P. Dubal, R. Holze, *Energy*, **2013**, *51*, 407, (b) D. P. Dubal, G. S. Gund, R. Holze, H. S. Jadhav, C. D. Lokhande, C. J. Park, *Electrochim. Acta*, **2013**, *103*, 103, (c) Q. Wang, X. Wang, B. Liu, G. Yu, X. Hou, D. Chen, G. Shen, *J. Mater. Chem. A*, **2013**, *1*, 2468

[4] (a) N. A. Choudhury, A. K. Shukla, S. Sampath, S. Pitchumani, *J. Electrochem. Soc.*, **2006**, *153*, A614, (b) P. Sivaraman, A. Thakur, R. K. Kushwaha, D. Ratna, A. B. Samui, *Electrochem. Solid-State Lett.* **2006**, *9*, A435.

[5] (a) C. D. Lokhande, D. P. Dubal, O. S. Joo, *Curr. Appl. Phys.*, **2011**, *11*, 255, (b) L. Yu, G. Zhang, C. Yuan, X. W. Lou, *Chem. Commun.*, **2013**, *49*, 137 (c) K. Xu, W. Li, Q. Liu, B. Li, X. Liu, L. An, Z. Chen, R. Zou, J. Hu, *J. Mater. Chem. A*, **2014**, *2*, 4795

[6] (a) W. Wei, X. Cui, W. Chen, D. G. Ivey, *Chem. Soc. Rev.*, **2011**, *40*, 1697, (b) D. P. Dubal, J. G. Kim, Y. Kim, R. Holze, W. B. Kim, *Energy Technol.*, **2013**, *1*, 125, (c) M. T. Lee, W. T. Tsai, M. J. Deng, H. F. Cheng, I. W. Sun, J. K. Chang, *J. Power Sources*, **2010**, *195*, 919

[7] (a) X. L. Wang, A. B. Yuan and Y. Q. Wang, *J. Power Sources*, **2007**, *172*, 1007, (b) C. C. Hu, Y. T. Wu and K. H. Chang, *Chem. Mater.*, **2008**, *20*, 2890, (c) J. P. Ni, W. C. Lu, L. M. Zhang, B. H. Yue, X. F. Shang, Y. Lv, *J. Phys. Chem. C*, **2009**, *113*, 54, (d) N. A. Tang, X. K. Tian, C. Yang and Z. B. Pi, *Mater. Res. Bull.*, **2009**, *44*, 2062

[8] (a) X. Y. Liu, Y. Q. Zhang, X. H. Xia, S. J. Shi, Y. Lu, X. L. Wang, C. D. Gu, J. P. Tu, *J. Power Sources*, **2013**, *239*, 157, (b) G. S. Gund, D. P. Dubal, S. B. Jambure, S. S. Shinde, C. D. Lokhande, *J. Mater. Chem. A*, **2013**, *1*, 4793, (b) W. Yang, Z. Gao, J. Ma, X. Zhang, J. Wang, J. Liu, *J. Mater. Chem. A*, **2014**, *2*, 1448

[9] (a) D. P. Dubal, G. S. Gund, R. Holze, C. D. Lokhande, *J. Power Sources*, **2013**, *242*, 687, (b) D. P. Dubal, R. Holze, *J. Power Sources*, **2013**, *238*, 274

[10] (a) H. Jiang, T. Zhao, C. Li, J. Ma, *J. Mater. Chem.*, **2011**, *21*, 3818, (b) J. Xiao, S. Yang, *RSC Adv.*, **2011**, *1*, 588

[11] (a) T. Brousse, M. Toupin, R. Dugas, L. Athouel, O. Crosnier, D. Belanger, *J. Electrochem. Soc.*, **2006**, *153*, 2171, (b) O. Ghodbane, J. L. Pascal, F. Favier, *ACS Appl. Mater. Interfaces*, **2009**, *1*, 1130

[12] (a) S. Devaraj, N. Munichandraiah, *J. Phys. Chem. C*, **2008**, *112*, 4406 (b) F. Y. Cheng, Y. Su, J. Liang, Z. L. Tao, J. Chen, *Chem. Mater.*, **2010**, *22*, 898

[13] (a) D. W. Wang, F. Li, H. M. Cheng, *J. Power Sources*, **2008**, *185*, 1563, (b) H. Inoue, Y. Namba, E. Higuchi, *J. Power Sources*, **2010**, *195*, 6239.

[14] G. S. Gund, D. P. Dubal, B. H. Patil, S. S. Shinde, C. D. Lokhande, *Electrochim. Acta*, **2013**, *92*, 205

[15] (a) F. Deng, L. Yu, G. Cheng, T. Lin, M. Sun, F. Ye, Y. Li, *J. Power Sources*, **2014**,

251, 202, (b) X. F. Lu, D. J. Wu, R. Z. Li, Q. Li, S. H. Ye, Y. X. Tong, G. R. Li, *J. Mater. Chem. A*, **2014**, *2*, 4706

[16] (a) C. Yu, C. Masarapu, J. Rong, B. Wei, H. Jiang, *Adv. Mater.*, **2009**, *21*, 4793, (b) M. Kaempgen, C. K. Chan, J. Ma, Y. Cui, G. Gruner, *Nano Lett.*, **2009**, *9*, 1872.

[17] Z. J. Fan, J. Yan, T. Wei, L. J. Zhi, G. Q. Ning, T. Y. Li, F. Wei, *Adv. Funct. Mater.*, **2011**, *21*, 2366

[18] (a) Q. T. Qu, Y. S. Zhu, X. W. Gao, Y. P. Wu, *Adv. Energy Mater.*, **2012**, *2*, 950. (b) Q. T. Qu, L. Li, S. Tian, W. L. Guo, Y. P. Wu, R. Holze, *J. Power Sources*, **2010**, *195*, 2789.

[19] J. T. Zhang, J. W. Jiang, H. L. Li, X. S. Zhao, *Energy Environ. Sci.*, **2011**, *4*, 4009.

[20] Y. M. He, W. J. Chen, X. D. Li, Z. X. Zhang, J. C. Fu, C. H. Zhao, E. Q. Xie, *ACS Nano*, **2013**, *7*, 174.

[21] Y. T. Wang, A. H. Lu, H. L. Zhang, W. C. Li, *J. Phys. Chem. C*, **2011**, *115*, 5413.

[22] Q. T. Qu, Y. Shi, S. Tian, Y. H. Chen, Y. P. Wu, R. Holze, *J. Power Sources*, **2009**, *194*, 1222,

[23] T. Cottineau, M. Toupin, T. Delahaye, T. Brousse, D. Belanger, *Appl. Phys. A: Mater. Sci. Process.*, **2006**, *82*, 599.

[24] G. H. Yu, L. B. Hu, M. Vosgueritchian, H. L. Wang, X. Xie, J. R. McDonough, X. Cui, Y. Cui, Z. N. Bao, *Nano Lett.*, **2011**, *11*, 2905.

[25] L. J. Deng, G. Zhu, J. F. Wang, L. P. Kang, Z. H. Liu, Z. P. Yang, Z. L. Wang, *J. Power Sources*, **2011**, *196*, 10782

[26] D. W. Wang, F. Li, H. M. Cheng, *J. Power Sources*, **2008**, *185*, 1563

[27] C. Z. Yuan, B. Gao, X. G. Zhang, *J. Power Sources*, **2007**, *173*, 606

[28] H. Chen, L. F. Hu, Y. Yan, R. C. Che, M. Chen, L. M. Wu, *Adv. Energy Mater.*, **2013**, *3*, 1636.

[29] M. C. Liu, L. Kang, L. B. Kong, C. Lu, X. J. Ma, X. M. Li, Y. C. Luo, *RSC Adv.*, **2013**, *3*, 6472.

Figure captions

Fig. 1 SEM images of three different nanostructures of MnO_2 (a, b) Mn-Nr (c, d) Mn-Nw and (e, f) Mn-Nn, at two different magnifications, respectively.

Fig. 2 TEM images of MnO_2 (a) Mn-Nr (b) Mn-Nw and (c) Mn-Nn with corresponding SAED pattern of Mn-Nn samples.

Fig. 3 (a-c) XRD patterns of three different nanostructures of MnO_2 such as Mn-Nr, Mn-Nw and Mn-Nn, respectively.

Fig. 4 (a-c) Nitrogen adsorption/desorption isotherm of Mn-Nr, Mn-Nw and Mn-Nn samples, respectively (d) corresponding pore size distribution plots.

Fig. 5 (a-c) Cyclic voltammetry curves of Mn-Nr, Mn-Nw and Mn-Nn electrodes at different scanning rates, respectively, (d-f) Galvanostatic charge/discharge (CD) curves of Mn-Nr, Mn-Nw and Mn-Nn electrodes at different current densities, respectively.

Fig. 6 (a-c) CV curves of Mn-Nr//rGO, Mn-Nw//rGO and Mn-Nn//rGO all solid state asymmetric cells at different scan rates, respectively. (d-f) Galvanostatic charge/discharge (CD) curves of Mn-Nr//rGO, Mn-Nw//rGO and Mn-Nn//rGO asymmetric cells at different current densities, respectively,

Fig. 7 (a) Variation of specific capacitance of Mn-Nr//rGO, Mn-Nw//rGO and Mn-Nn//rGO all solid state asymmetric cells with scan rate (b) The specific power versus specific energy of Mn-Nr//rGO, Mn-Nw//rGO and Mn-Nn//rGO asymmetric cells in a Ragone plot.

Fig. 8 Variation of capacity retention of (A) Mn-Nr//rGO, (B) Mn-Nw//rGO and (C) Mn-Nn//rGO all solid state asymmetric cells with number of cycles at 100 mV/s scan rate.

Fig. 9 Schematic representation of all solid state asymmetric (Mn-Nn//rGO) devices with PVA-H_3PO_4 gel electrolyte along with charge-potential profiles

Table of content

Schematic representation of all solid state asymmetric (Mn-Nn//rGO) devices with PVA-H_3PO_4 gel electrolyte along with charge-potential profiles

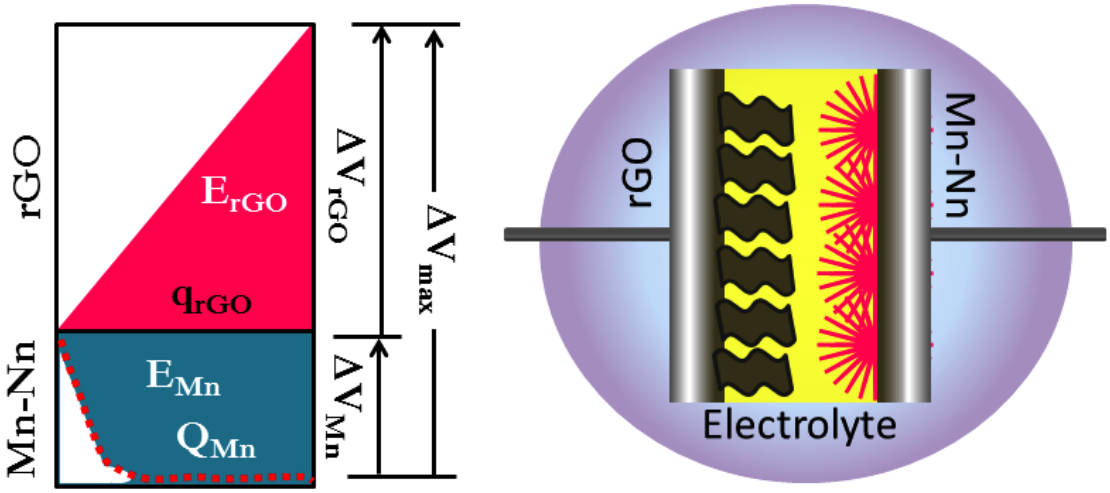

Figures
Click here to download Manuscript: Figures.doc

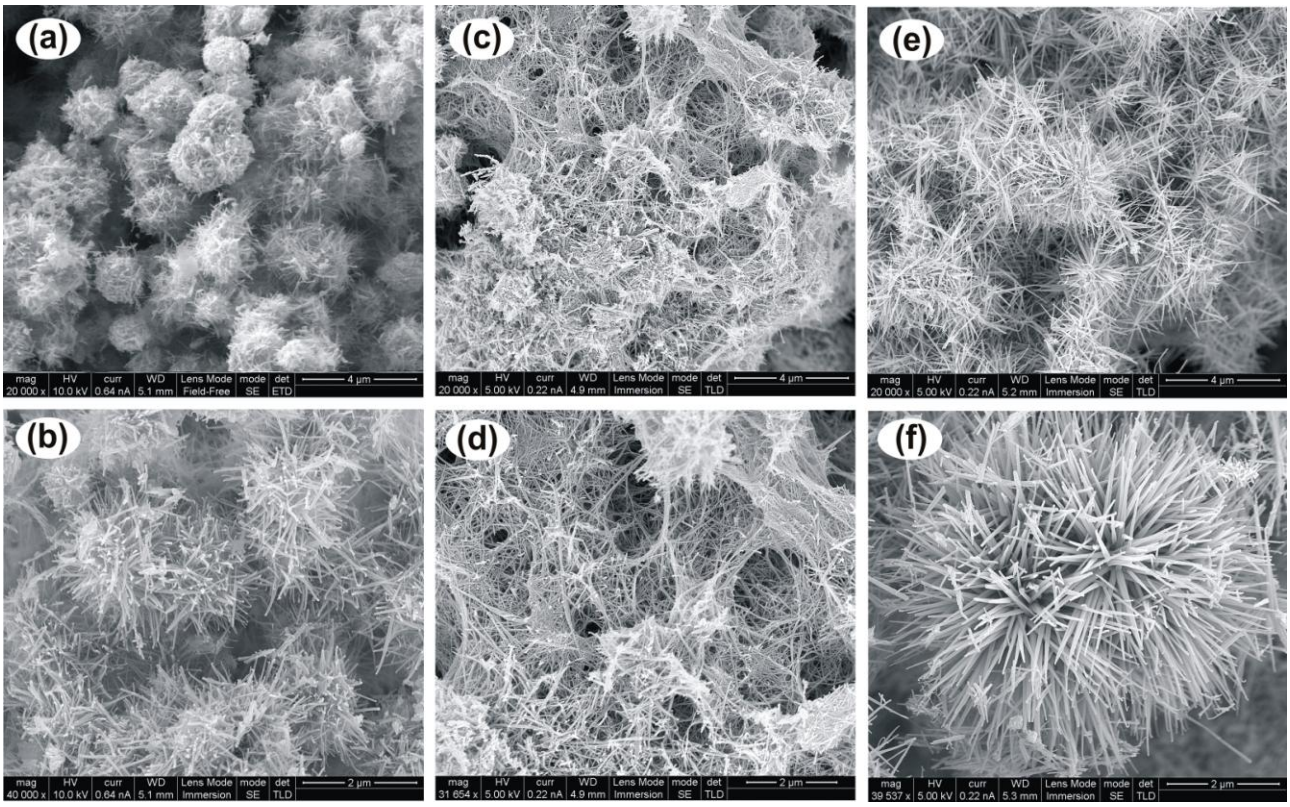

Fig. 1

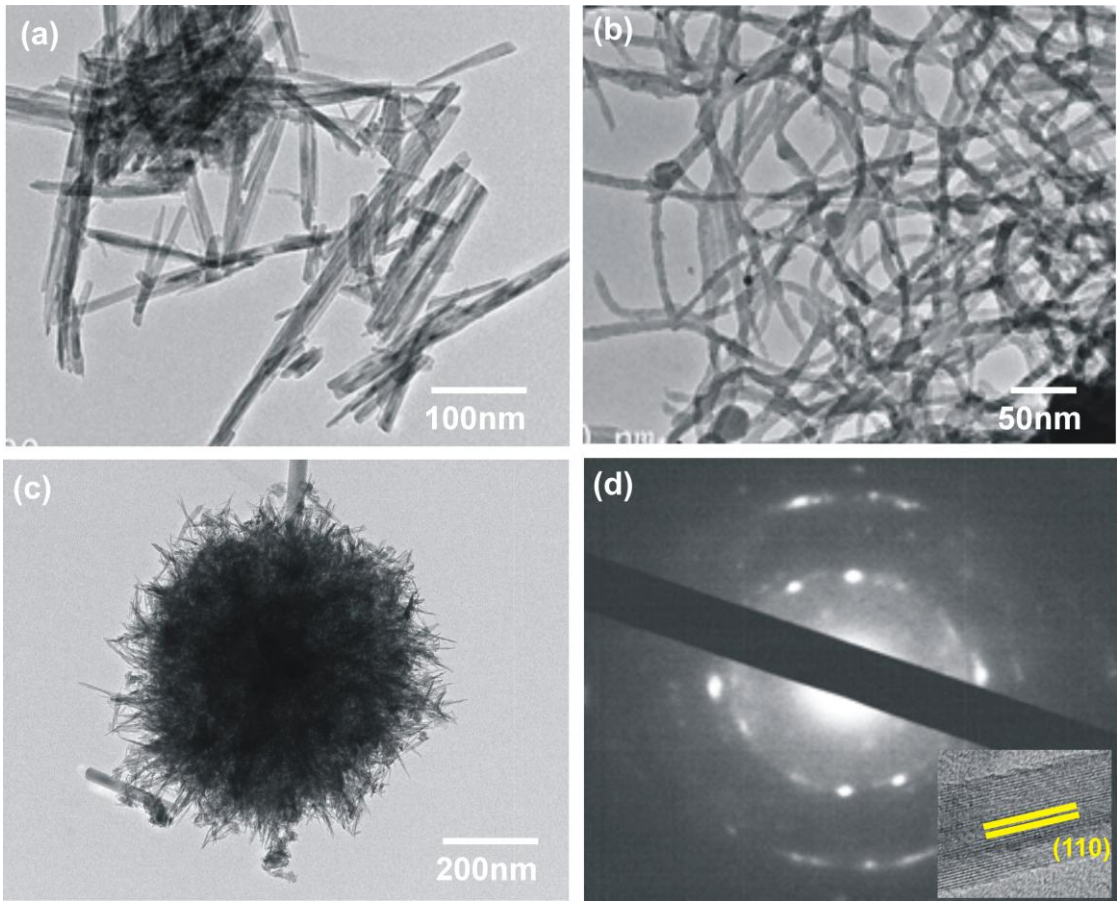

Fig. 2

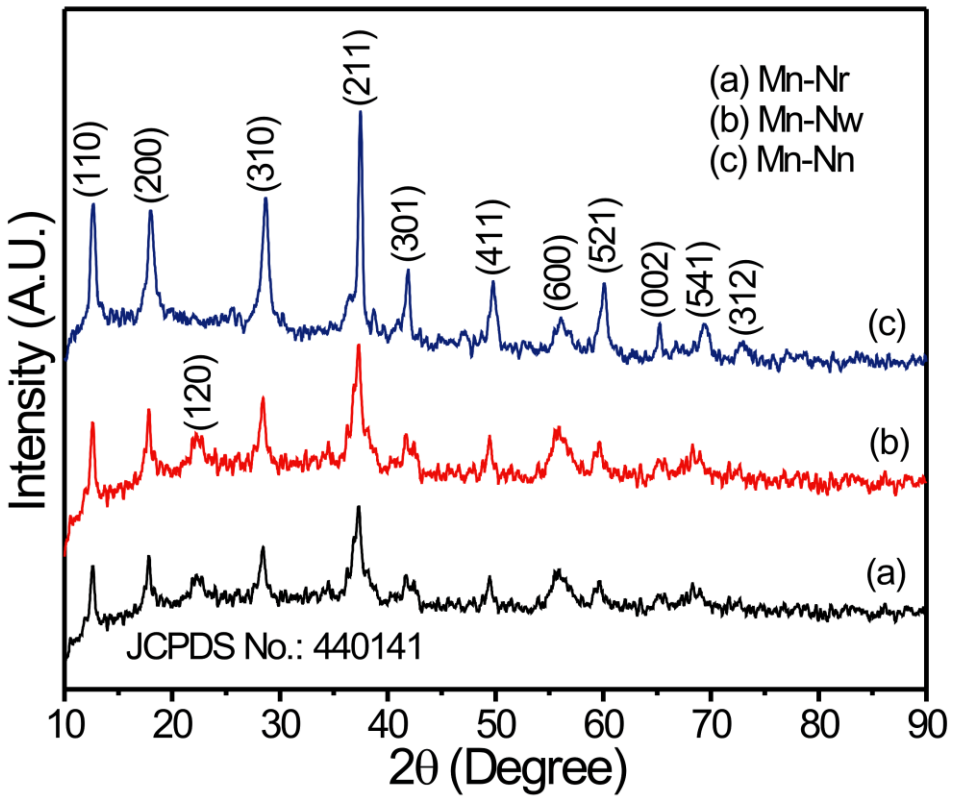
(a) Mn-Nr
(b) Mn-Nw
(c) Mn-Nn
(110)
(200)
(310)
(211)
(301)
(411)
(600)
(521)
(002)
(541)
(312)
(120)
(c)
(b)
(a)
JCPDS No.: 440141
Intensity (A.U.)
10
20
30
40
50
60
70
80
90
2θ (Degree)

Fig. 3

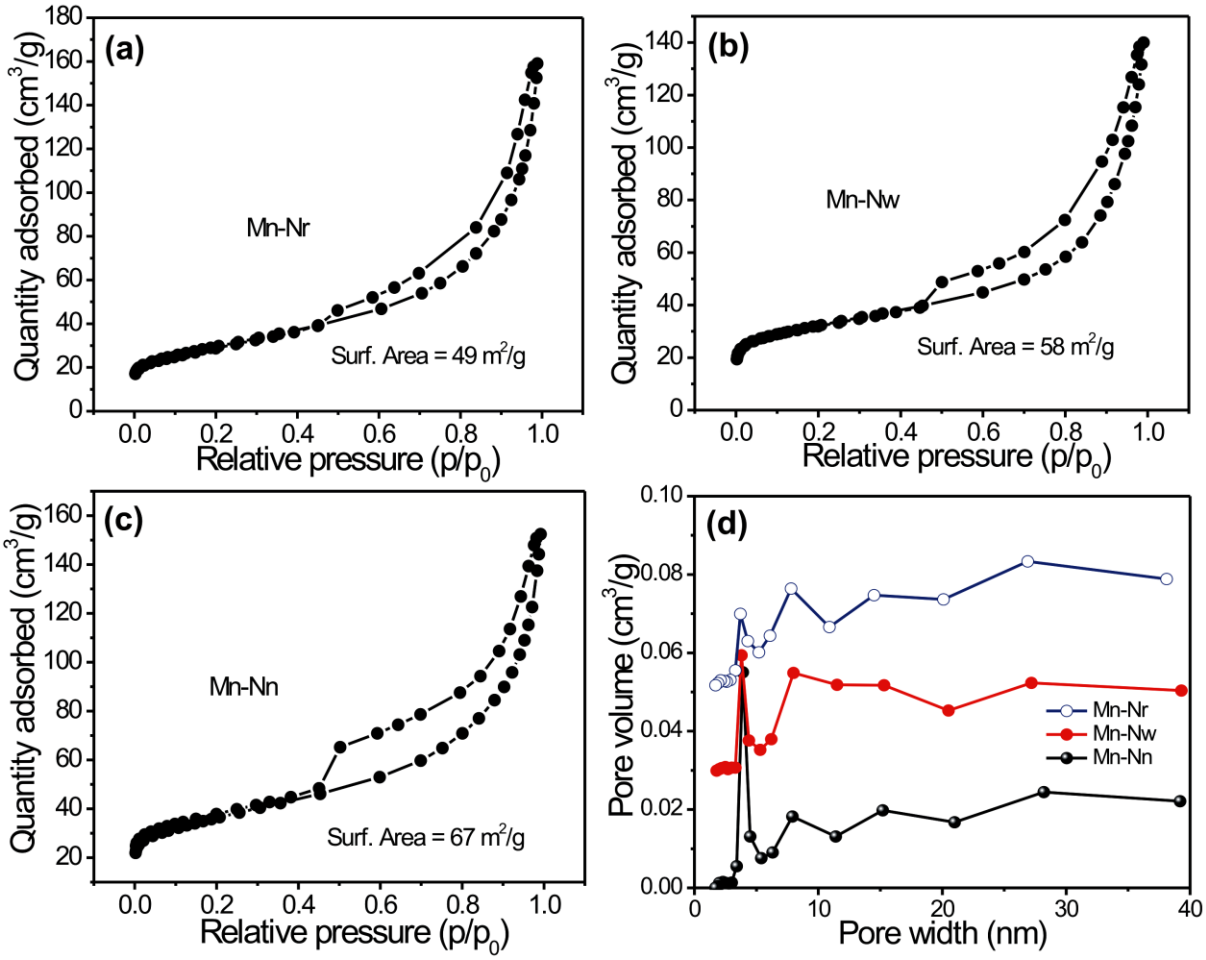
(a)
Mn-Nr
Surf. Area = 49 m²/g
Quantity adsorbed (cm³/g)
Relative pressure (p/p0)
(b)
Mn-Nw
Surf. Area = 58 m²/g
Quantity adsorbed (cm³/g)
Relative pressure (p/p0)
(c)
Mn-Nn
Surf. Area = 67 m²/g
Quantity adsorbed (cm³/g)
Relative pressure (p/p0)
(d)
Pore volume (cm³/g)
Pore width (nm)
Mn-Nr
Mn-Nw
Mn-Nn

Fig. 4

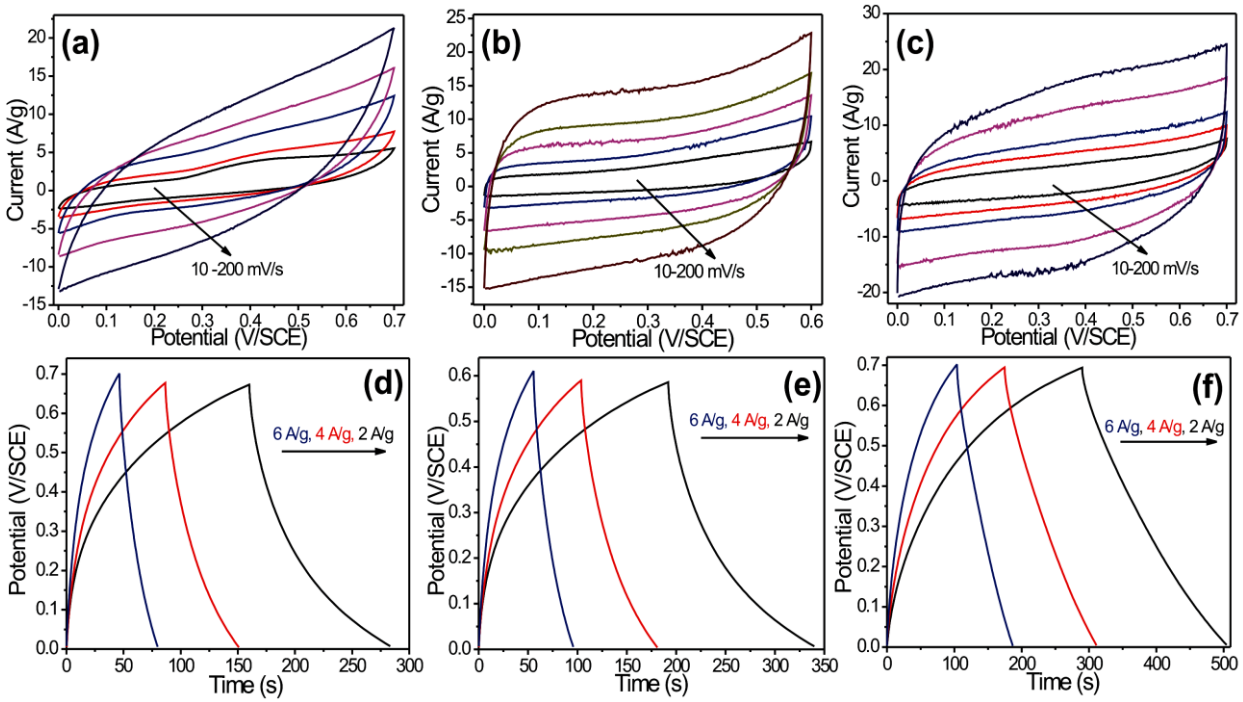
(a)
(b)
(c)
(d)
(e)
(f)
Current (A/g)
Potential (V/SCE)
10 -200 mV/s
10-200 mV/s
Potential (V/SCE)
Time (s)
6 A/g, 4 A/g, 2 A/g

Fig. 5

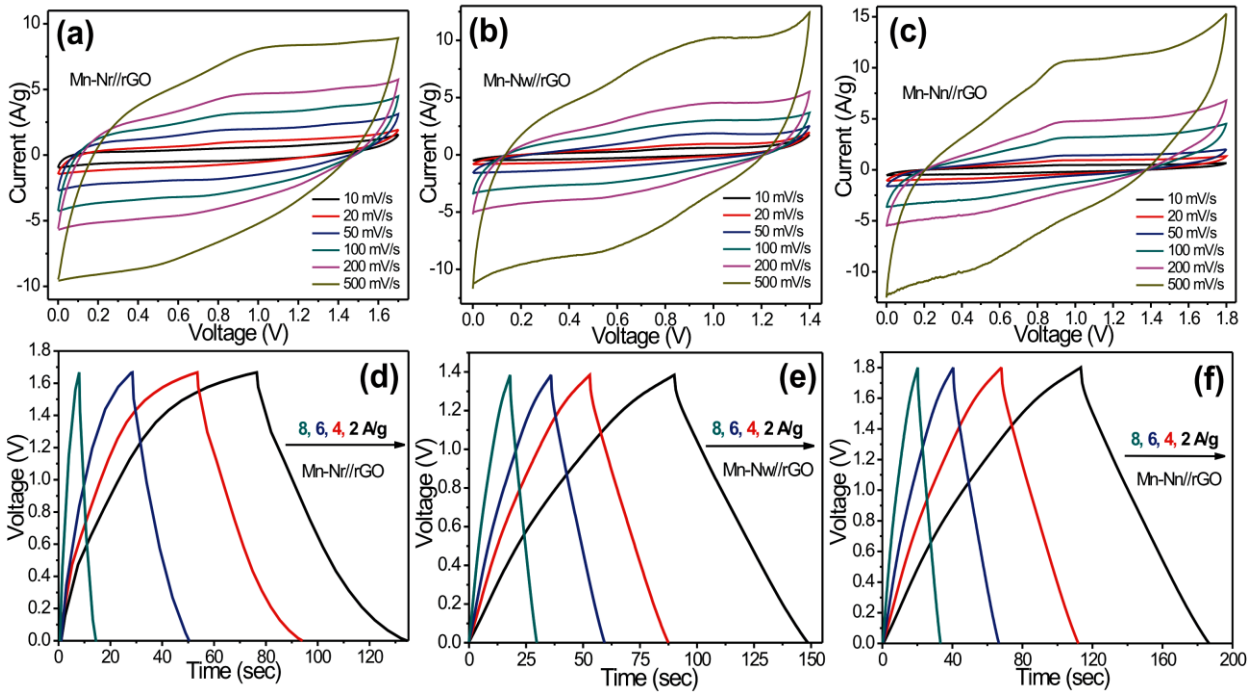
(a)
Mn-Nr//rGO
Current (A/g)
Voltage (V)
10 mV/s
20 mV/s
50 mV/s
100 mV/s
200 mV/s
500 mV/s
(b)
Mn-Nw//rGO
Current (A/g)
Voltage (V)
10 mV/s
20 mV/s
50 mV/s
100 mV/s
200 mV/s
500 mV/s
(c)
Mn-Nn//rGO
Current (A/g)
Voltage (V)
10 mV/s
20 mV/s
50 mV/s
100 mV/s
200 mV/s
500 mV/s
(d)
8, 6, 4, 2 A/g
Mn-Nr//rGO
Voltage (V)
Time (sec)
(e)
8, 6, 4, 2 A/g
Mn-Nw//rGO
Voltage (V)
Time (sec)
(f)
8, 6, 4, 2 A/g
Mn-Nn//rGO
Voltage (V)
Time (sec)

Fig. 6

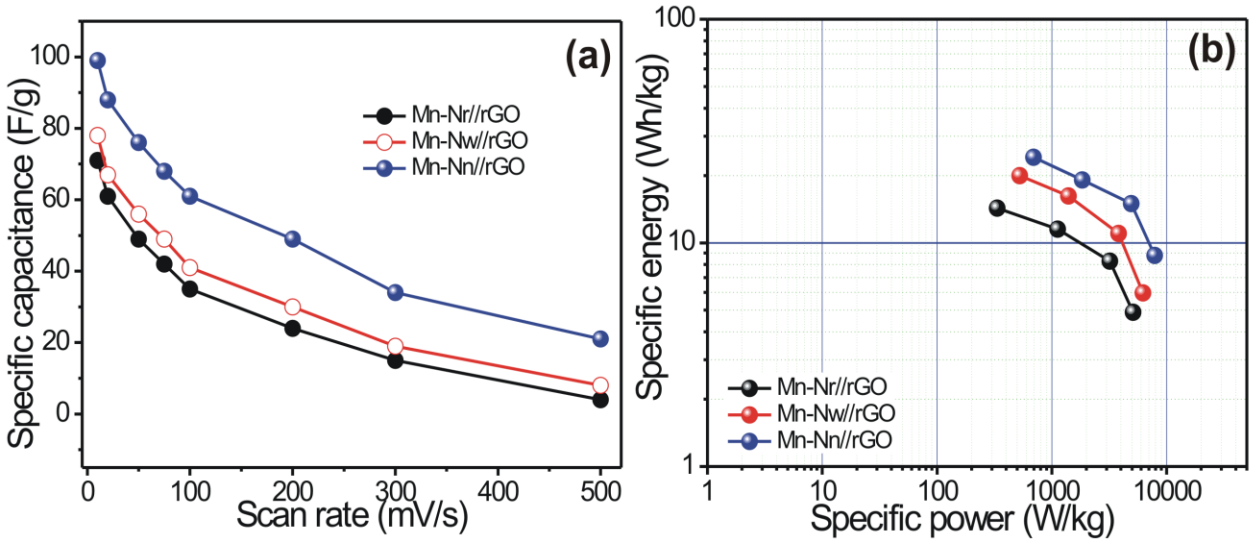
(a)
Specific capacitance (F/g)
Scan rate (mV/s)
Mn-Nr//rGO
Mn-Nw//rGO
Mn-Nn//rGO
(b)
Specific energy (Wh/kg)
Specific power (W/kg)
Mn-Nr//rGO
Mn-Nw//rGO
Mn-Nn//rGO

Fig. 7

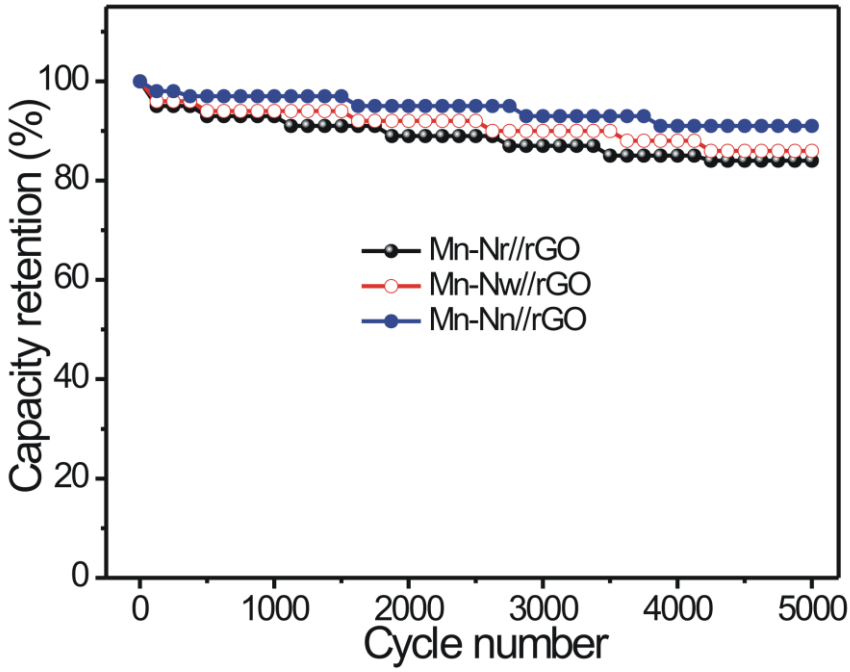
Capacity retention (%)
100
80
60
40
20
0
0
1000
2000
3000
4000
5000
Cycle number
Mn-Nr//rGO
Mn-Nw//rGO
Mn-Nn//rGO

Fig. 8

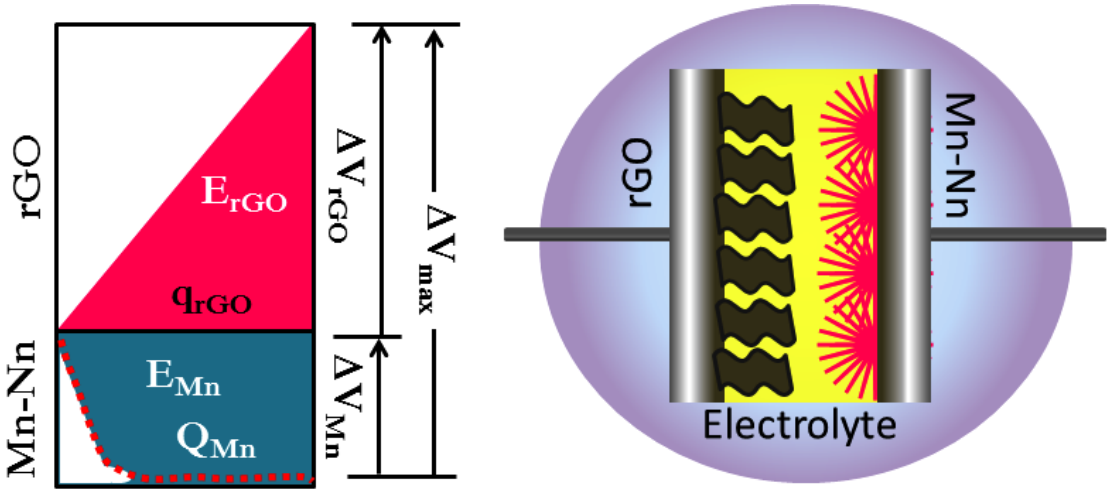
rGO
Mn-Nn
E_{rGO}
q_{rGO}
E_{Mn}
Q_{Mn}
ΔV_{rGO}
ΔV_{max}
ΔV_{Mn}
rGO
Mn-Nn
Electrolyte

Fig. 9

Supporting Information

Click here to download Supporting Information: Supporting information.doc